Vortex Shedding as a Mechanism for Free Emboli Formation in Mechanical Heart Valves

Danny Bluestein
State University of New York at Stony Brook,
Stony Brook, NY 11794-8181

Edmond Rambod

Morteza Gharib

California Institute of Technology,
Pasadena, CA 91125

The high incidence of thromboembolic complications of mechanical heart valves (MHV) limits their success as permanent implants. The thrombogenicity of all MHV is primarily due to platelet activation by contact with foreign surfaces and by nonphysiological flow patterns. The latter include elevated flow stresses and regions of recirculation of blood that are induced by valve design characteristics. A numerical simulation of unsteady turbulent flow through a bileaflet MHV was conducted, using the Wilcox k–ω turbulence model for internal low-Reynolds-number flows, and compared to quantitative flow visualization performed in a pulse duplicator system using Digital Particle Image Velocimetry (DPIV). The wake of the valve leaflet during the deceleration phase revealed an intricate pattern of interacting shed vortices. Particle paths showed that platelets that were exposed to the highest flow stresses around the leaflets were entrapped within the shed vortices. Potentially activated, such platelets may tend to aggregate and form free emboli. Once formed, such free emboli would be convected downstream by the shed vortices, increasing the risk of systemic emboli. [S0148-0731(00)01202-4]

Background

Implantation of a MHV imposes a neodisease with serious potential side effects. Some of these complications are common to all valves, and some are more usual with certain types of valves. Bleeding complications are related to the need for anticoagulant therapy, a risk shared by all mechanical valves. Thromboembolism is defined as the blocking of a blood vessel by an embolus that has broken away from a thrombus (a clot of blood) at its site of formation, and is common to all valves [1,2]. The hemodynamic properties of prosthetic heart valves induce hemolysis (disintegration of blood constituents) and thromboembolic occurrences that are related to flow-induced damage or activation of corpuscular blood components, resulting in late complications that are sometimes fatal or require re-operation [3]. Thrombosis may lead to local occlusion of the prosthesis or thromboemboli, which may cause critical obstruction to blood flow in distant organs. Cardioembolism, or embolic stroke, comprises about 70 percent of all systemic embolism, which is the most serious complication of heart valve replacement [3].

Thrombi form *in vivo* as a pathologic consequence of activating hemostasis under variable flow conditions. Platelets are very small (1–2 μm in diameter) anucleate blood corpuscles whose primary role is in the process of hemostasis is the forming of multicellular aggregates in a blood clot. The thrombotic process involves a complex integrated interaction among surface, platelets, and activated coagulation factors that form a localized thrombus. The thrombogenicity of all MHV's is primarily due to an activation of platelets. Upon activation, platelets undergo dramatic morphological and biochemical changes, resulting in shape change (extrusion of pseudopodia), aggregation, granule secretion, and clot retraction [4]. Current valve designs still generate flow locales that are characterized by high shear stresses, turbulent fluctuations, and regions of recirculation of blood and stasis. Those, in turn, enhance the risk of thrombus formation by inducing platelet activation, aggregation, and deposition [1]. The tilting disk type valves are prone to massive thrombus formation, particularly along the perimeter of the minor outflow regions, including the hinge mechanism and the pivot well. Figliola and Mueller [5] estimated the hemolytic and thrombogenic potential of occluder MHV's and indicated that cites of thrombus formation correlate with regions of slow-moving separated flow. A passage of a small fragment of thrombus from a mitral prosthesis to the left atrium may cause mitral valve occlusion [2].

Fluid stresses in prosthetic heart valves were extensively measured *in vitro* in the late 1970's and through the 1980's using laser-Doppler anemometry (LDA). Implicit in all of these studies was the hypothesis that blood damage occurs predominantly during forward peak flow. In recent years, studies with Bjork–Shiley tilting disk valves [6], St. Jude valve [7], and Medtronic Hall tilting disk valve [8] indicated that turbulent jets induced by regurgitant flow through the closed valve produce stresses that can be an order of magnitude higher than those found in the forward flow phase. Work that elucidate the dynamics of hemolysis and the actual thrombus formation on the valves are scarce. However, Lamson et al. [9] studied the relative blood damage of MHV's by dividing the flow cycle into three phases: (*a*) forward flow through an open valve, (*b*) rapid valve closure, and (*c*) regurgitant back flow through a closed valve. Each phase is believed to contribute toward injury to formed elements in the blood.

Platelet survival is decreased in all patients with prosthetic heart valves. The direct correlation between platelet lysis, valve surface area, and systemic embolization implies the formation of platelet thromboemboli on the valve surface [10]. Presumptive evidence of thromboembolism includes emboli seen by funduscopic examination or thrombi observed by angiography or echocardiography [11]. Dewanjee [12] was able to quantify platelet thrombosis in valve prostheses by measuring *in vivo* the deposition of radioactive labeled platelets using scintigraphy, and quantified *in vitro* the number of adherent platelets on the components of a mitral valve prostheses using a gamma counter.

Over the last decade, substantial evidence has been accumulated suggesting that flow-induced forces and convective mass transfer can be extremely important in modulation of the molecular mechanisms of platelets. Turitto et al. [13] broke down the factors that affect thrombus growth to three categories: (1) fluid mechanical factors, (2) blood-related factors, and (3) vascular factors. Deposition of platelets onto artificial surfaces tends to increase with increasing shear [14]. Adhesion of platelets to a surface is greatly enhanced by prior activation, as the platelet loses

Contributed by the Bioengineering Division for publication in the JOURNAL OF BIOMECHANICAL ENGINEERING. Manuscript received by the Bioengineering Division December 9, 1998; revised manuscript received November 3, 1999. Associate Technical Editor: J. B. Grotberg.

its disk shape by the extrusion of pseudopodia, which in turn increases the collision frequency among each other and with the surface [15]. Fluid mechanical factors implicated in thrombus formation through platelet activation and subsequent deposition include high rates of shear and deformation, turbulence, and areas of flow stagnation or recirculation that are characterized by low shear and longer retention time [16]. Thrombus formation is preceded by platelet activation in areas of high shear flow, followed by platelet deposition onto the wall in areas of stasis and recirculation. A decrease in platelet deposition onto a Lexan surface was observed in the throat region of a stenosis, supplemented by an increase in the downstream recirculation region [17]. Folie and McIntire [16] investigated the effect of flow and shear on platelets aggregate size and geometry in whole blood using epifluorescent video microscopy. Their group further visualized and quantified thrombus formation through measurements of platelet aggregation [18].

Combining data from several researchers with phenomenological studies of platelet response under constant shear stress and varying duration, Hellums et al. [19] depicted a locus of incipient shear-related platelet serotonin release on a shear stress-exposure time plane, which is commonly used as a standard for platelet activation threshold. Sutera et al. [20] showed that pulsed exposure resulted in more platelet aggregation than continuous exposure. In addition, Purvis and Giorgio [21] showed that platelets exposed to elongational stresses are activated at lower shear levels and tend to form larger aggregates. Stress histories (shear, turbulent, and elongational) were studied along platelet paths in a stenosis, and a *level of activation* parameter was defined for the platelets [22].

Heart valves induce flow disturbances that play a role in blood constituents activation and damage. Vortex shedding is a complex flow phenomenon of interacting vortices in the wake of bluff bodies [23]. Vortex shedding in the presence of free-stream disturbances, turbulence, and periodic pulsation, is directly relevant to flow past mechanical heart valves. In flow past mechanical heart valves, there are several locales where shear layers are generated, particularly in the interface between the wakes induced by the valve leaflets and the accelerating jets through the valve orifices. Such shear layers are prone to produce vortex shedding through a process of inviscid instability. The inviscid instability of a shear layer is associated with its roll up into discrete vortices, which may then undergo secondary instability and become turbulent; the discrete vortices may also pair up due to subharmonic resonance. As the flow passes through the valve leaflets and accelerates through the orifice, eddy rings periodically roll up into vortex trains and tear away from the edge. Downstream, these vortex trains undergo transition through secondary instability and become turbulent [24,25].

Vortex shedding was postulated in flow past heart valves [26], and observed experimentally in the wake of mechanical heart valves leaflets [7,27]. Huang et al. [28] conducted the first high-resolution unsteady laminar flow numerical simulation in the wake of a tilting disk heart valve that revealed the complex behavior of vortex shedding. They estimated the ''apparent'' Reynolds stress (nonturbulent) associated with the vortex shedding to be as high as 3900 dyn cm^{-2}. While this stress level is not expected to damage blood cells because the spatial scales associated with vortex shedding are too large, turbulent stresses are expected to induce damage because turbulent eddies cascade energy to ever smaller spatial scales while dissipating it. Vortex shedding may also play a dominant role in the aggregation of activated platelets that are trapped in these small-scale dynamic recirculation zones. It is postulated that these shed vortices are the origin of cerebrovascular microemboli associated with prosthetic heart valves, by providing activated platelets and clotting factors an optimal environment for microthrombi formation.

Methods

Numerical Methods. Computational Fluid Dynamics (CFD) modeling of unsteady turbulent flow was employed. The blood was modeled as a viscoelastic fluid, with yield stress of 0.1 s^{-1} and a changing viscosity with physiological blood properties (data taken from [29]), approximating $\rho = 1.056\ g/cm^3$, $\mu = 3.5$ cPoise, and $\nu = 0.035\ cm^2/s$ at elevated shear levels. Potential platelet activation and aggregation sites were studied through the local flow dynamics (areas of elevated flow stresses, turbulent flow patterns, converging streamlines, particle paths leading to recirculation zones, the dynamics of shed vortices). The cardiac output was 5.5 L/min and the heart rate was 72 bpm (820 ms heart cycle).

The numerical simulations were conducted using the FIDAP CFD package (Fluent Inc., Lebanon, NH) that utilizes a finite element procedure, using the Galerkin form of the Method of Weighted Residuals [30] to solve the Navier–Stokes equations:

$$\rho\left(\frac{fu_i}{ft} + u_j u_{i,j}\right) = \sigma_{ij,i} + \rho f_i \tag{1}$$

$$\frac{f\rho}{ft} + (\rho u_j)_j = 0 \tag{2}$$

In turbulent flows all variables in the governing NS equations are decomposed into average values and small fluctuations, e.g., $u = \overline{U} + u'$, where the overbar denotes time-average and the prime denotes fluctuation from this average. When this is substituted into the equations and time averaging is performed, a resulting extra variable is introduced to the stress terms, i.e., the Reynolds stresses $\rho\overline{u'v'}$. To close the governing equations with the extra variables, the two-equation $k-\varepsilon$ turbulence model is traditionally employed. In the $k-\varepsilon$ turbulence model, the turbulence field is characterized in terms of the turbulent kinetic energy k and the viscous dissipation rate of turbulent kinetic energy ε, which are defined as

$$k = \frac{1}{2}\overline{u_i u_i}; \quad \varepsilon = \overleftrightarrow{\nu}\,\overline{u_{i,j}u_{i,j}} \tag{3}$$

Two transport equations, one for k and one for ε, are obtained from the NS equations and the new system of equations is then solved. While this approach is very efficient and accurate for high-Re flows, it may produce inferior predictions for some low-Re flows. As physiological flows are exclusively in the low-Re range, the innovative Wilcox $k-\omega$ model [31], which is primarily intended for simulating globally low-Re internal flows (Re$<$10,000) was employed. In this model, the turbulent dissipation is related to the turbulent kinetic energy via the simple expression $\varepsilon = \omega k$, where ω is the turbulent frequency. The turbulent scales u_t and δ_t are related through dimensional analysis to k and ω according to $u_t \propto \sqrt{k}$ and $\delta_t \propto \sqrt{k}/\omega$. The turbulent viscosity is obtained from the $k-\omega$ relation; $\mu_t = \mu\rho k/\omega$, and the $k-\omega$ transport equations are solved.

The geometry simulated was two-dimensional, incorporating a bileaflet St. Jude Medical MHV implanted in the aortic position. A progressive mesh density in the axial direction was applied to the inlet region, so that flow conditions at the inlet could evolve from a uniform plug flow velocity profile to a fully developed turbulent velocity profile (where turbulence prevailed). A physiological pressure gradient was applied at the inlet and zero stress condition at the outlet. The entrance and exit lengths were conservatively chosen as 10 diameters upstream and 12 diameters downstream correspondingly ($D = 27$ mm), so that the turbulent velocity profiles could be fully established proximal to the valve and no outlet effects could be noticeable downstream. The progressive density and resolution of the finite elements mesh in the radial direction was dictated by the need in the $k-\omega$ model of the first grid point away from the walls to be in the vicinity of $y^+ \leq 1$ (y^+

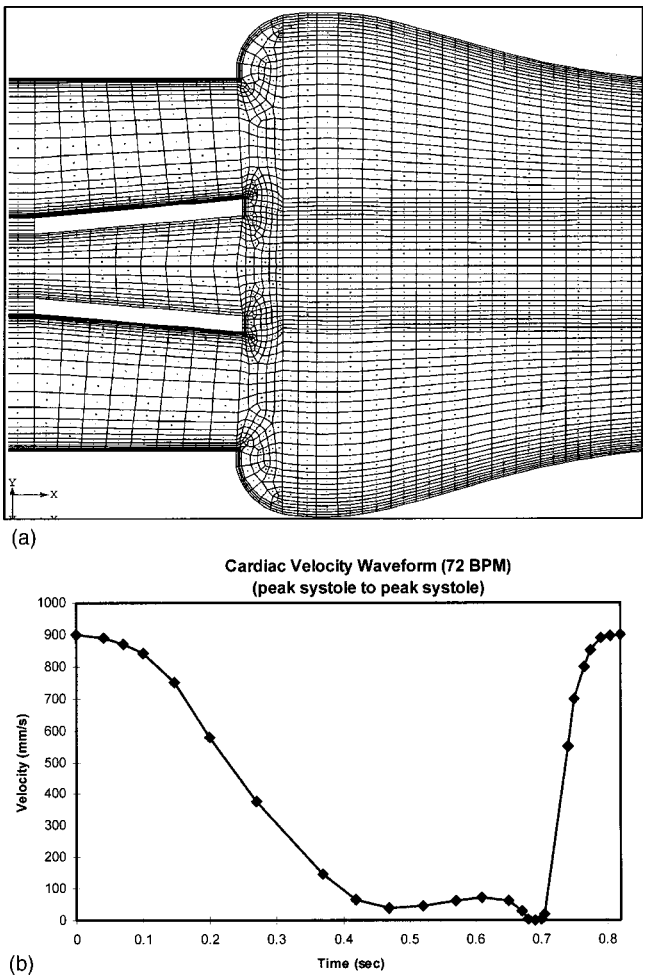

Fig. 1 (*a*) Details of the numerical mesh in the valve area, (*b*) inlet velocity waveform

being the nondimensional viscous sublayer height). The height of Δ, the first grid point from the wall, was computed in the following manner [31,32]:

$$\omega = \frac{6\nu}{C_2 \Delta^2} \tag{4}$$

With a computed characteristic near-wall turbulent dissipation rate of $\varepsilon = 50{,}613\ \mathrm{mm^2/s^3}$ and $C_2 = 0.8333$, the $\varepsilon = \omega k$ relation with a typical turbulent kinetic energy of $k = 4050\ \mathrm{mm^2/s^2}$ yielded a characteristic turbulent frequency of $\omega = 125\ \mathrm{s^{-1}}$. These values put Δ at a characteristic value of 140 μm, which was used to determine the minimal mesh density in the vicinity of the wall. After establishing the numerical results to be independent of mesh density in all directions, the two-dimensional mesh, solved in half of the flow domain (assuming symmetry around the *x* axis), consisted of some 4500 quadrilateral elements each containing 9 nodes, i.e., 40,500 computational nodes. The resulting mesh is shown in Fig. 1(*a*), in the vicinity of the valve.

The choice of a transient analysis time integration algorithm is governed by its rate of convergence and sensitivity to variations in the initial conditions. The choice of the segregated version of the solver, combined with a hybrid relaxation method and streamline upwinding was successful in achieving convergence for the demanding combination of a transient problem and turbulence modeling. The inlet velocity waveform chosen mimics a typical physiological waveform at a heart rate of 72 beats per minute (bpm), and is shown in Fig. 1(*b*). In order to achieve faster convergence, computation started with peak systolic flow conditions (approximately 90 cm/s axial velocity at the inlet) and proceeded through the deceleration and following acceleration phases. The typical initial time step was 0.125×10^{-3} s, requiring some 6560 time steps to complete the computation of one cardiac cycle (820 ms).

Turbulent particle paths were computed using a stochastic model [33], which simulates the influence of turbulence on particle trajectories. In this model the instantaneous velocities in the carrier phase are used to solve the particle velocities. These instantaneous characteristics are computed by adding random fluctuations obtained from the $k-\omega$ simulation, in the following manner:

$$U_\infty = \overline{U} + \lambda u'; \quad u' = \sqrt{(2/3k)} \tag{5}$$

where λ is a random number between -1 and 1, sampled from a normal distribution. The motion of each particle is traced as it interacts with a succession of turbulent eddies. The interaction time with one eddy is limited to the eddy life time, *Te*, or the time needed for the particle to traverse the eddy, T_t, defined by:

$$Te = \frac{Le}{\sqrt{2/3k}}; \quad T_t = -2 \ln\left(1 - \frac{Le}{\tau |U_\infty - U_p|}\right) \tag{6}$$

where *Le* is the eddy characteristic size $Le = c_\mu^{3/4} k^{3/2}/\varepsilon$ and τ is the particle relaxation time. U_p in Eq. (6) is the particle velocity. In FIDAP the Lagrangian approach of dispersed two-phase flow, or particulate two-phase flow, is employed, where the particulate phase is dispersed in the ''carrier'' liquid phase. The information transfer between phases is accounted for by their momentum, energy, and mass gain or losses along particle paths. For a particle of density ρ_p and diameter D_p the relevant governing equation is:

$$\frac{du_p^i}{dt} = \frac{1}{\tau}(u_i - u_p^i) + f_p^i \tag{7}$$

where u_p^i is the particle velocity, u_i is the velocity of the fluid carrier phase, f_p^i is the combination of forces acting on the particle, and τ is a relaxation time model that takes into account viscosity of the fluid, the particle drag coefficient, and the Reynolds number.

Finally, as regards the particulate phase, the kinematic equation from which the particle trajectory is obtained is:

$$\frac{dx_p^i}{dt} = u_p^i \tag{8}$$

The *i* index refers to the coordinates directions, so that in this two-dimensional simulation the two velocity components are used to compute the trajectory of the particle. After each interaction, a new fluctuation is assumed to act on the particle, i.e., the particle enters a new eddy. Unlike laminar flow numerical simulations, which yield exactly the same particle path when a particle is repeatedly injected at a certain point in the flow field, the combination of turbulence modeling and a stochastic model for turbulent particle paths computations results in a different particle path for each run, as should be the case under turbulent flow conditions.

DPIV Measurements. A prototype bileaflet aortic valve was constructed using a pair of 27 mm Pyrolytic carbon leaflets of St. Jude Medical mechanical prosthesis inserted in a precisely machined transparent housing ring to allow for flow measurements using DPIV (Digital Particle Image Velocimetry). The valve was mounted in the aortic position of a noncompliant test section of the *in vitro* flow loop (Fig. 2). The test section mimicked the geometry of the aortic root, with the sinuses of Valsalva machined into a 95 mm×50 mm×50 mm rectangle piece of Lucite, providing flat surfaces and matched index of refraction to allow noninvasive optical measurements. The inflow to the aortic valve was specifically designed to create flow uniformity and eliminate any flow separation effects. A compliance chamber was located distal

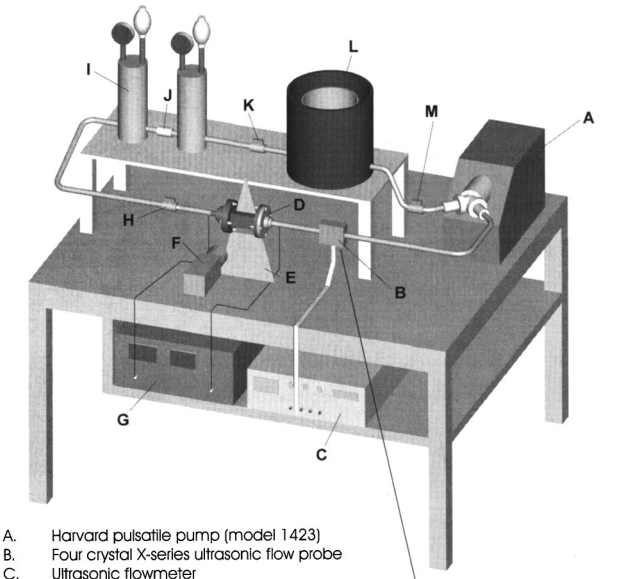

Fig. 2 Schematics of the Caltech pulse duplicator system. The system has been designed for investigating different features of aortic valve flows and consists of three major components: (1) test section, (2) pulsatile pump, (3) lumped compliance and peripheral resistance. A prototype bileaflet valve was constructed using a pair of 27 mm Pyrolitic Carbon leaflets mounted in a precisely machined transparent housing to allow Digital Particle Image Velocimetry. A typical aortic flow waveform is shown.

to the valve to allow valve closing and control the pressure. A 5 liter constant-head reservoir was located between the compliance chamber and the pulsatile pump (Fig. 2). Pulsatile flow was generated by a Harvard 1423 blood pump at a flow rate of 5.0 liter/min, pulse rate of 70 bpm, and systolic time of 35 percent. A solution of 36 percent by volume glycerol in deionized water with a bulk viscosity of 3.5*cp* was used as a blood analog fluid. A solution of 20 g/L sucrose ($C_{12}H_{22}O_{11}$ glucose-α-1,2 fructose) was added to the fluid to match the refraction index of Lucite, with a negligible effect on the blood analog fluid viscosity at 37°C. The temperature of the liquid in the entire system was monitored continuously by using a sensitive autotuned temperature controller (OMEGA CN9000A) that kept the temperature constant at 37°C throughout the system. An average afterload of 100 mmHg was maintained throughout the experiment. A 4 Crystal *X*-Series clamp-on ultrasonic flow probe (Transonic Systems Inc., Ithaca, NY) was placed between the pump and the test chamber and was connected to a T110 flowmeter (Transonic Systems, Inc., Ithaca, NY). A ± 1 V output from the flowmeter, which was displayed digitally on the flowmeter panel in L/min, was filtered and transferred to the A/D board (MacADIOS ADPO, GW Instruments), which was interfaced with the main data acquisition system (Superscope II, GW Instruments) for display and further analysis. A typical acquired aortic flow waveform is shown in Fig. 2.

DPIV measurements of the transaortic flow were conducted at the Cardiovascular Fluid Dynamics Research Laboratory, California Institute of Technology, using a double pulse 25 mJoule YAG laser (New Wave, Sunnyvale, CA), CCD camera (768×484 pixels), frame grabber (Forster Sys. Engr., Irvine, CA), and image processing software. The DPIV technique is capable of providing a quantitative two-dimensional picture of displacement of particles and the velocity vector field of the flow. In this method the fluid is seeded with particles (40 μm silver-coated microspheres) and single exposure images of the particles illuminated by a laser light sheet are recorded using the CCD video camera. The displacements of the particles are obtained by locally cross-correlating sequential images, and the velocity vector fields are computed from the known timing of the laser pulses. The cross-correlation function of the two samples is calculated using FFT techniques. The displacement of the cross-correlation peak provides the average spatial shift of the particles in each subsample pair. Detailed description of the method can be found in Willert and Gharib [34].

Results and Discussion

Numerical Results. The flow past the valve during the deceleration phase was characterized by periodic vortex shedding (von Kármán vortex street) in the wake of the valve leaflets. Typical velocity vectors during the deceleration phase (105 ms after peak systole) are shown in Fig. 3. Three jets are formed; one jet was formed past the central orifice of the valve between the valve leaflets, and two jets are formed between the upper surfaces of the leaflets and the aortic wall. The wake of the valve reveals an intricate pattern of shed vortices that roll on top of each other, and extend as far as twice the leaflet length downstream. Five such vortices are easily discernible in the wake. A small part of the flow below the leaflet is recirculating, effectively confining the central jet to a smaller cross section, thus reducing deceleration effect that could have resulted from the diverging cross section between the leaflets in their fully open position. Consequently, the acceleration of the jet through the central orifice is maintained. These effects are best seen in Fig. 4, where several axial velocity profiles (U) in different cross sections (105 ms after peak systole) are superimposed. At $x = -18.3$ mm, approximately 5 mm before the leaflet ($x = 0$ at the tip of the leaflet, the length of the leaflet is 13.47 mm), the velocity profile has a typical top hat distribution, with a center hump that precedes the pressure buildup at the stagnation point of the leaflet's leading edge. The velocity profile is

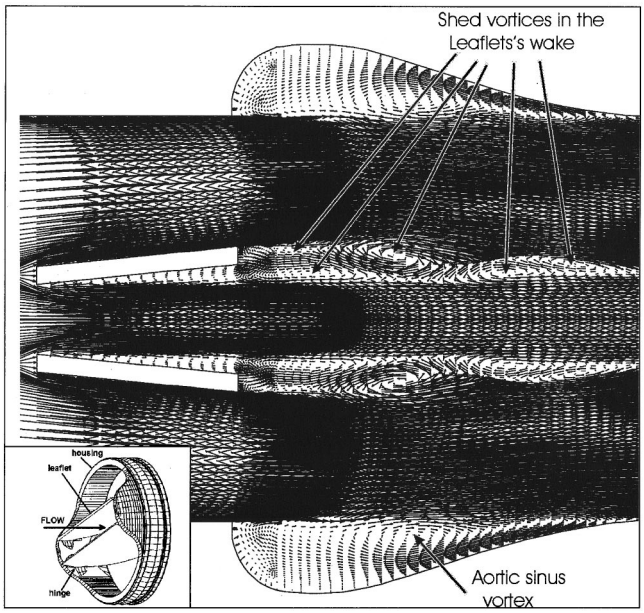

Fig. 3 Velocity vectors depicting the shed vortices in the wake of a St. Jude Medical bileaflet MHV during the deceleration phase (105 ms after peak systole). The leaflets (side view cross section) are shown in the fully open position.

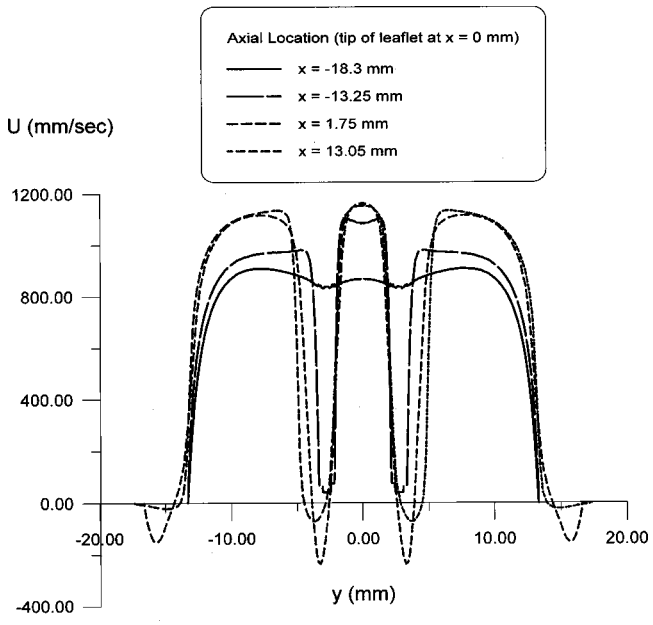

Fig. 4 The development of axial velocity profiles past the valve and in the wake (105 ms after peak systole)

clearly turbulent (Re=6172). At the leading edge of the leaflet ($x=-13.25$ mm), the flow is diverged above and below the leaflet, creating a typical tri-peaked velocity profile of a central jet (between the leaflets) and two circumferential jets (above the leaflets). Accordingly, the flow is accelerated, and the velocity gradients ($\partial U/\partial y$) become steeper. At $x=1.75$ mm (downstream from the tip of the leaflet), the acceleration of the flow is evident by an almost 50 percent higher peak velocities (approximately 1200 mm/s, as compared to approximately 800 mm/s proximal to the leaflet). Recirculation zones, characterized by negative velocities, are created between the leaflets. Those in turn effectively confine the jets to a smaller cross-sectional area, thus maintaining the flow acceleration. The velocity gradients are getting steeper, translating into higher shear stresses ($\tau=\mu\partial U/\partial y-\rho\overline{u'v'}$). At $x=13.05$ mm distal to the leaflet tip, well into the leaflet's wake, the recirculation velocities are stronger, and the confinement of the jet is maintained.

The acceleration of the flow along the upper and lower surfaces of the leaflet entails pronounced inertial effects; the higher velocity layer slides over the lower velocity layer, and the shear layer formed between the two layers rolls up into vortex trains. This phenomenon, which is well recognized in the wake of bluff bodies and around sharp corners, was less evident in flow past mechanical heart valves because of the lack of numerical and experimental resolution that would have enabled capturing the fine details of these vortices.

The dynamics of the shed vortices during the deceleration phase is depicted in Fig. 5, from 85 ms after peak systole to 142 ms after peak systole. At $T=0.85$ ms, three elongated vortices can be seen, one issuing from the upper surface of the leaflet, and a train of two from the lower surface. At $T=97$ ms, this vortex triplet is carried downstream, and a new, stronger vortex, is formed, issuing from the upper surface. At $T=102$ ms, this vortex rolls on top of the preceding vortices in a vortex pairing fashion. This is a typical process in shear layer flows; any slight nonuniformity in strengths or spacing of two (or three) adjacent vortices induces them to roll up around each other. As the flow is turbulent, in the process some nonturbulent fluid is entrained, to which vorticity fluctuations are transferred by viscous diffusion. At $T=107$ ms, the vortex pair keeps growing while being swept downstream, while the pair of vortices issuing from the upper and lower surfaces of the leaflet gain strength and extend further downstream. Eventually, at $T=117$ ms, a similar vortex roll up ensues with this vortex pair being swept downstream ($T=142$ ms), while new vortices are constantly being formed at the tip of the leaflet.

It is interesting to notice the interaction of the wake of the shed vortices with the aortic sinus vortex. While in the natural aortic valve, the vortex in each of the three sinuses of Valsalva is taking part in the pushing of the open leaflet toward closure before diastole begins [35], in an implanted MHV these vortices plays only a marginal role in the valve dynamics. In the sequence shown in Fig. 5 (from 85 ms after peak systole to 142 ms after peak systole) the center of the sinus vortex moves back and forth in a periodic fashion, interacting with the wake of shed vortices. The periodic vortex shedding induces a strong frequency with its associated subharmonic frequency, characteristic of the vortex pairing process, as well as a possible superharmonic frequency. In order to identify dominant frequencies that characterize the vortex shedding, a FFT (fast Fourier Transform) of the velocity was conducted in several locations deemed pertinent in the shear layer that is formed between the wake and the jet flow above the leaflet (Fig. 6). Two energy peaks are clearly dominant, at 51 Hz and 14 Hz; the former is the fundamental shedding frequency, while the latter is a subharmonic vortex pairing frequency (the 14 Hz frequency, which is approximately a third of the fundamental frequency, may be an indication to a coalescence process of a vortex triplet, as seems to be the case in the sequence shown in Fig. 4). A higher frequency peak at 102 Hz is a superharmonic.

Examination of the aortic sinus vortex motion shows that the center of the vortex completes one period of back and forth motion in approximately 20 ms, which corresponds to the fundamental shedding frequency of 51 Hz. The development of the spectra downstream depicts the vortex pairing process, where at points *c* and *d*, where the vortex pairing takes place, the subharmonic frequency dominates the spectra. Downstream, at points $e-h$ (the end of the wake), the fundamental frequency loses energy as more energy is being transferred to the subharmonic. This is characteristic of a coalescence process between vortices, whereby the subharmonic wave is being reinforced through a nonlinear interaction with the fundamental wave.

The shear distribution past the valve and around the leaflet is depicted in Fig. 7. Two shear layers are formed around the leaflet, extending downstream to surround the wake. Another shear layer is formed along the upper wall, bordering the aortic sinus vortex. The highest shear levels are generated in the shear layers surrounding the leaflet and the wake, on account of the steep velocity gradients characterizing the jets above and below the leaflet. Platelets that are flowing around the leaflets are thus exposed to the highest stress levels. This is also the location where the flow accelerates, followed by a rapid deceleration in the wake region. Platelets that flow above or below the leaflet along particle paths that may lead them to entrapment within the vortices populating the wake would additionally experience strong deformation stresses. As the combination of shear and deformation stresses has been shown to activate platelets below the threshold of activation under pure shear [20,21], such platelets would probably be activated earlier in space and time, in the high-stress areas around the leaflets where the flow is unidirectional.

In order to establish whether platelets that are exposed to the highest stress levels while carried by the flow around the leaflets are entrapped at the leaflet's wake, platelet paths were computed around the leaflets. Particles were ''seeded'' above and below the leaflet, and a stochastic model [33] was used for the computation of the turbulent platelet paths, resulting in different path for each run. Such particle paths are characterized by jagged trajectories that are induced by the turbulent fluctuations along the particle trajectory. Characteristic platelet paths shown in Fig. 8, above and below the leaflet, clearly indicate that those paths that exposed the platelets to the highest shear levels led them to entrapment within the shed vortices in the wake of the leaflet. This happened repeat-

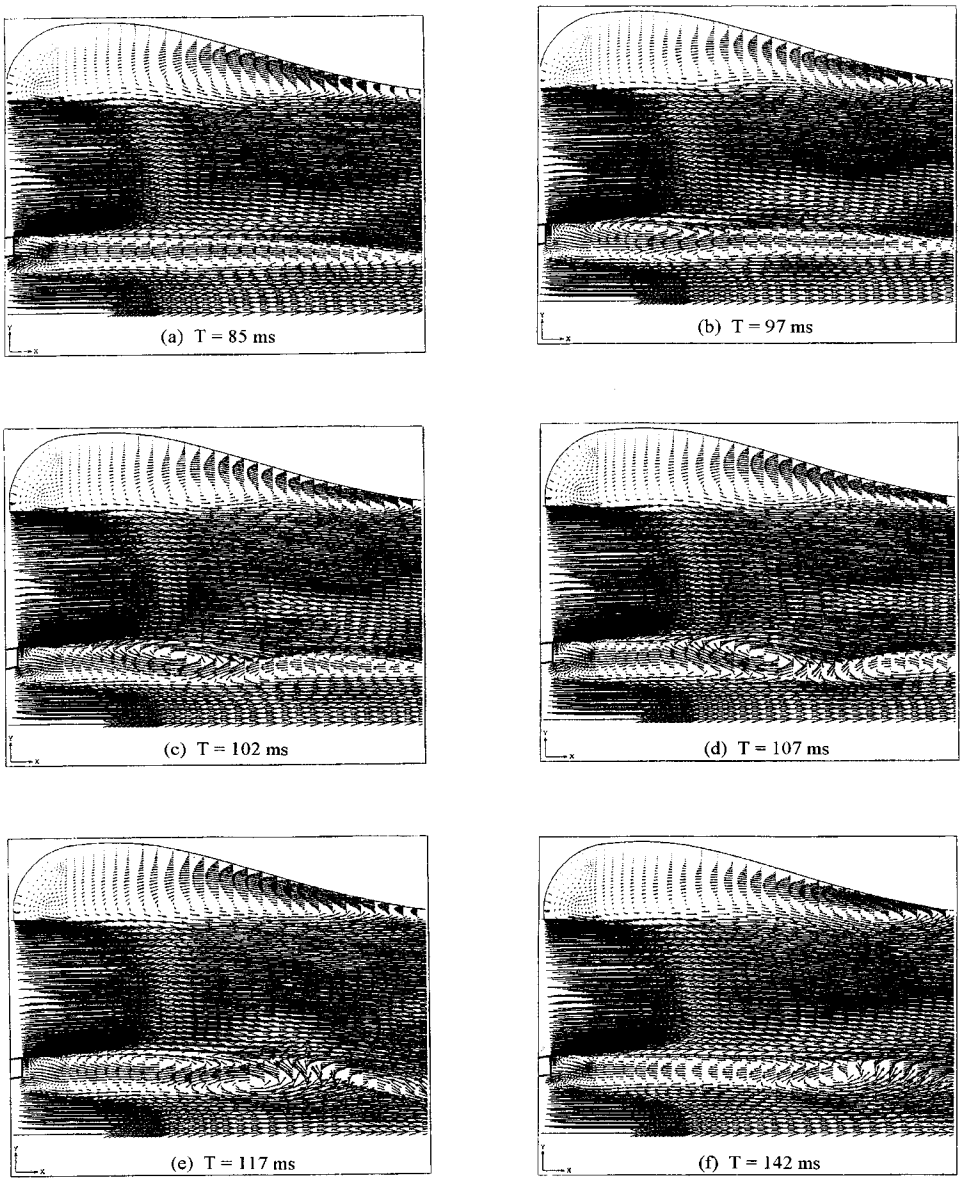

Fig. 5 Periodic vortex shedding coupled with vortex pairing during deceleration (85 ms to 142 ms after peak systole)

edly for both the particles that were seeded above and below the leaflet. These paths also expose the platelets to the highest deformation and turbulent stresses, indicating a higher incidence of platelet activation. Prior activation is known to increase the collision frequency among platelets, as the platelet loses its disk shape by the extrusion of pseudopodia, which increases its effective hydrodynamic volume by several folds [15]. The platelets are also more likely to bump into each other and form aggregates because of the turbulent fluctuations, as depicted by the turbulent platelet paths. The vortex pairing phenomenon that happens repeatedly within the wake promote the formation of larger platelet aggregates. Once formed, such free emboli would be convected downstream, as demonstrated by the convection of the shed vortices (Fig. 5).

Extending the concept of Hellums et al. [19] who depicted a platelet activation locus on a shear stress-exposure time domain, this group has developed the concept of *level of activation* of a platelet [22], which quantifies the shear stress history of an individual platelet along its trajectory. This is done by a summation of the product of the instantaneous values of the shear stresses and

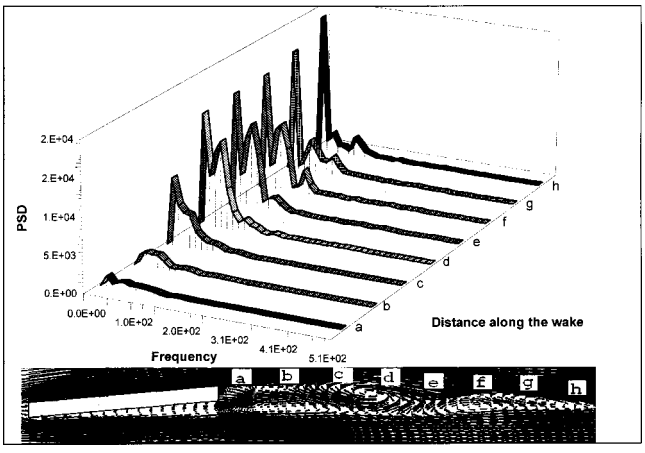

Fig. 6 Fundamental and subharmonic frequency peaks, characteristic of vortex coalescence, populating the velocity spectra in the leaflet's wake

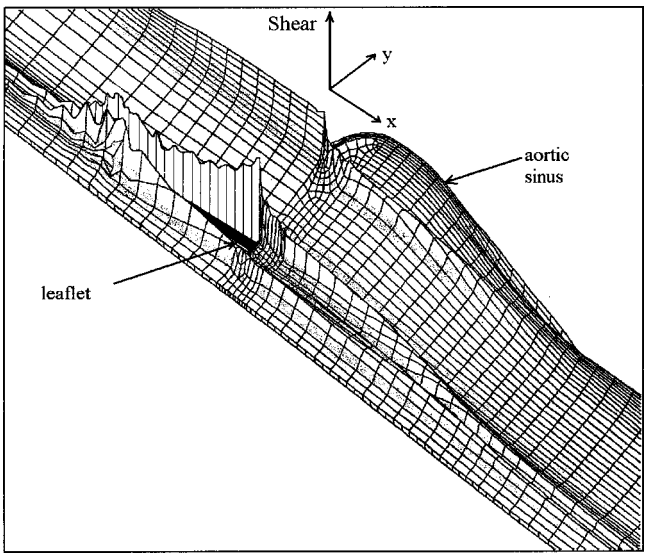

Fig. 7 Shear distribution around the valve's leaflet (67 ms after peak systole). Note the two shear layers that are formed around the leaflet, extending downstream to surround the wake.

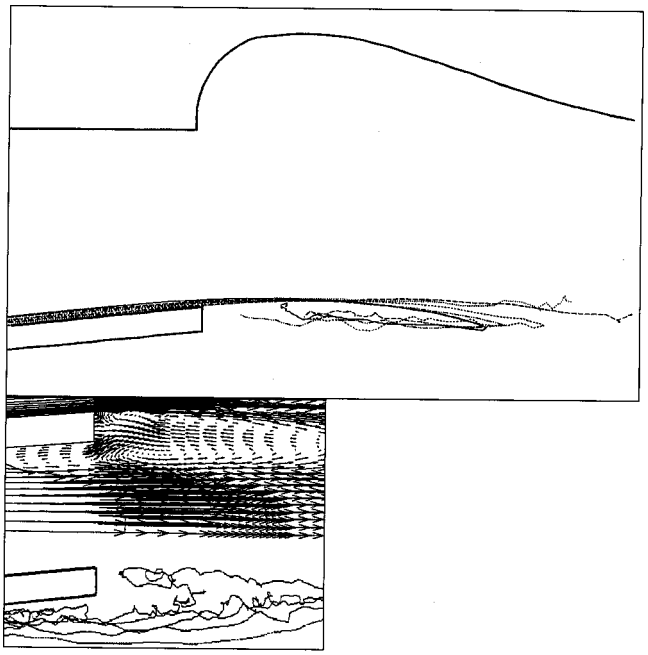

Fig. 8 Turbulent platelet paths through areas of highest stresses around the leaflet: above the leaflet (top) and below (bottom), leading to entrapment within the shed vortices in the leaflet's wake. The corresponding velocity vectors are shown (paths are computed from 165 ms to 419 ms after peak systole).

the exposure times along the platelet path ($\Sigma\{\tau\times\Delta t\}$). The level of activation parameter of a platelet along its path is presented in Fig. 9. Two representative platelet paths were chosen: one that passes through the regions of high shear stresses near the leaflet (Fig. 7) leading the platelet to entrapment within the shed vortices of the wake, and a second in which the platelet flows in the core flow region. The comparison of the level of activation of these two paths clearly demonstrates that the path around the leaflet gives rise to level of activation that is one order of magnitude

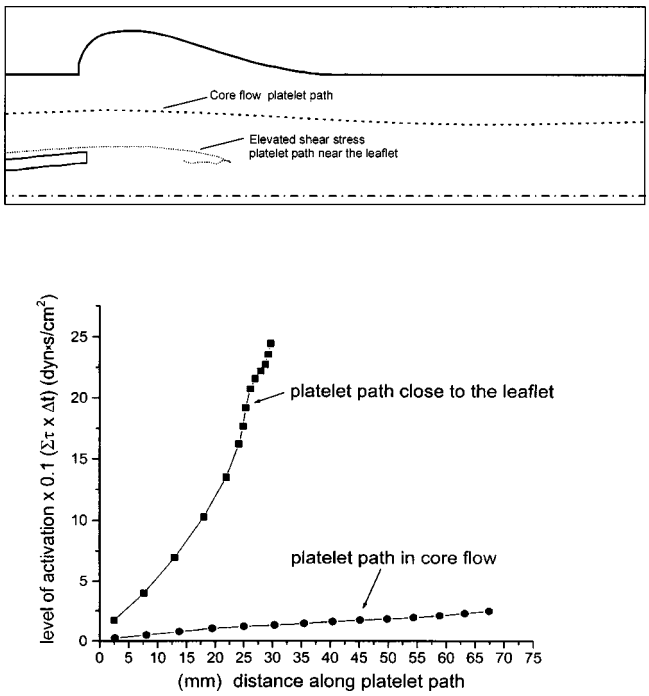

Fig. 9 Comparison between the shear stress history (level of activation) of a platelet that flows near the leaflet and gets trapped in the wake's vortices, and a platelet that flows in the core flow, where shear stress levels are relatively low. The two *level of activation* curves were computed along the corresponding platelet paths shown above.

larger than that of the core flow path. One can also notice an increase in the level of activation once the platelet is captured in the wake, because of the longer retention time.

DPIV Measurements

Figure 10(*a*) depicts the velocity vector field during peak systolic flow downstream of the aortic valve as measured in the *in vitro* flow loop (Fig. 2). The flow separated from the two leaflets and formed a trailing wake downstream, which was characterized by visible fluctuations in the velocity vectors. In addition to the velocity vector field, the level of the vorticity in the flow field is an important measure of the vortical flow components. Vorticity is defined as $\vec{\omega}=\nabla\times\vec{U}$, where for the measured 2D DPIV flow field, the vorticity is computed as $\omega=\partial v/\partial x-\partial u/\partial y$. The vorticity field in the two wakes extending from the tip of the leaflets downstream is clearly outlined in Fig. 10(*b*), where the vortices are depicted by the boundaries between dashed and solid isovorticity contours. The dashed contours represent counterclockwise rotation and the solid contours represent clockwise rotation. The width of the wake close to the leaflets was approximately 3 mm and the maximum local vorticity at the core of the vortices reached values as high as 550 s^{-1}, indicating the strong vortical structures that were generated by the shed vortices in the leaflets' wake. A zoom-in image on a single leaflet (shown from 0.05 cm distal to the leaflet's tip downstream) depicted with great detail the formation of shed vortices in the wake of the leaflet (Fig. 10(*a*)). The corresponding vorticity plot (Fig. 10(*b*)) depicts the contours of strong vorticity, which coincided with the centers of the vortices. Farther downstream, the wake became unstable and the vortices started to meander. The vortices and their locations were in very good agreement with the numerical results, validating the predictions of the turbulence model employed.

A comparison between the DPIV measurements and the numerical results is shown in Fig. 11, zooming in the wake of a single leaflet (105 ms after peak systole, from 0.05 cm to 1.2 cm

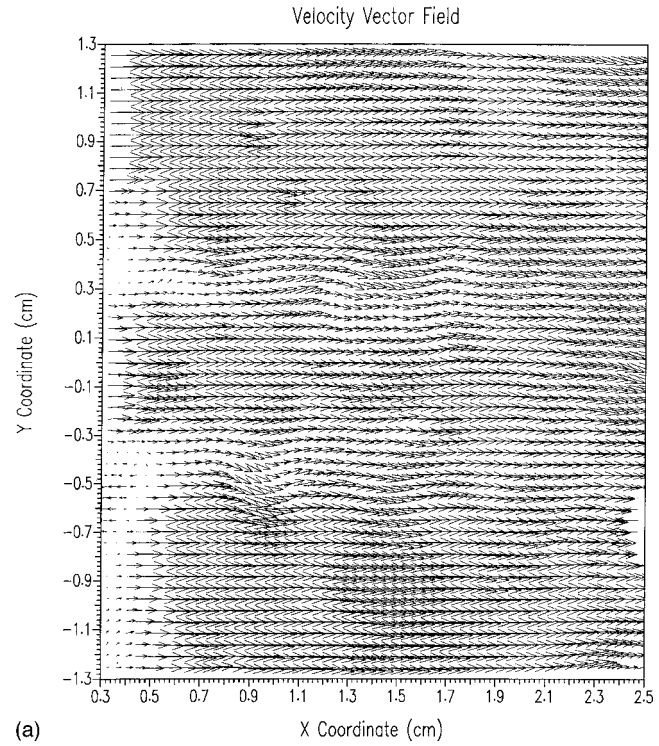

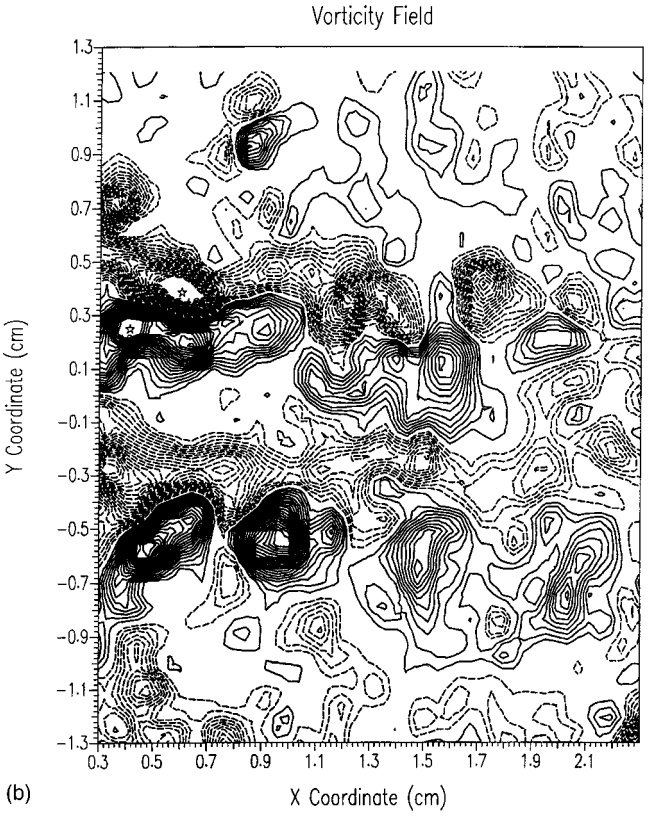

Fig. 10 (*a*) **DPIV measurements of the velocity vector field distal to the valve during peak systole. The tips of the leaflets are located at** $y = \pm 0.3$ **cm. The trailing wakes, extending from the two leaflets downstream, induce visible fluctuations on the velocity vectors.** (*b*) **Vorticity field distal to the valve during peak systole. Dashed contours represent counterclockwise rotation, and solid lines represent clockwise rotation.**

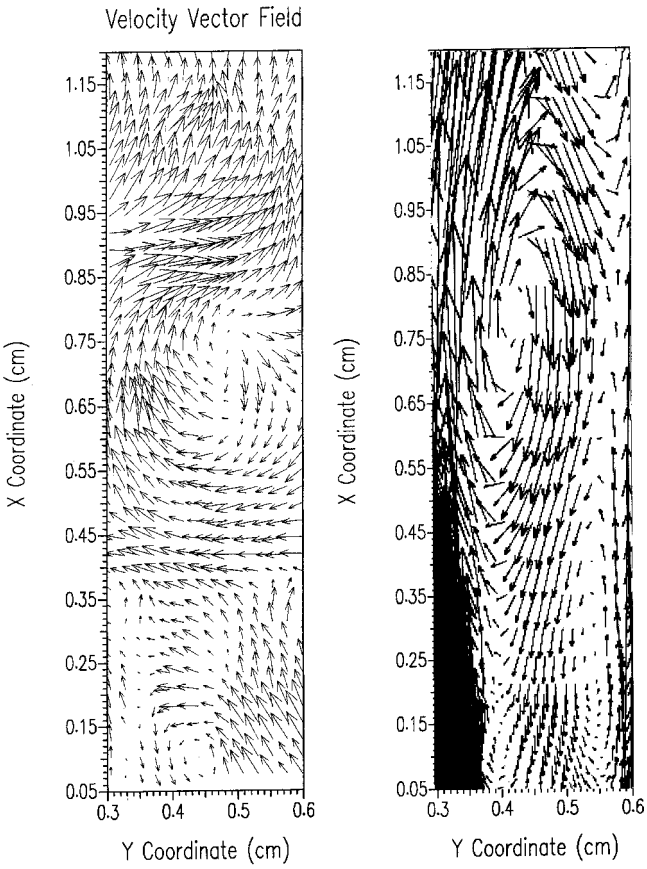

Fig. 11 Comparison between DPIV measurements and numerical results zooming in the wake of a single leaflet (105 ms after peak systole, from 0.05 cm to 1.2 cm distal to the tip of the leaflet)

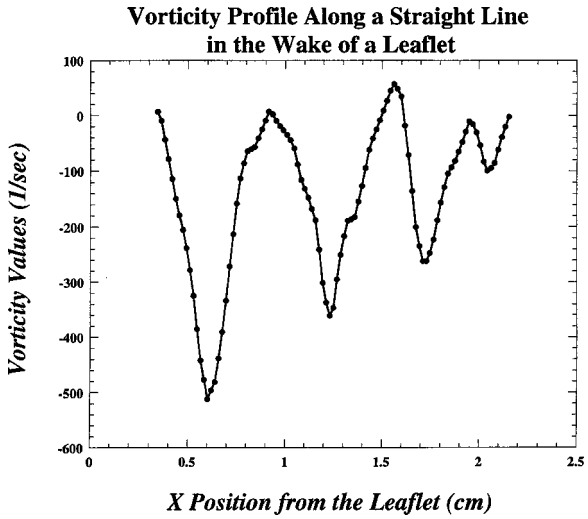

Fig. 12 Vorticity distribution in the wake, along a straight line from the leaflet tip. The vorticity alternates between positive and negative values (clockwise and counterclockwise rotation), typical of the "Karman vortex street" dynamics.

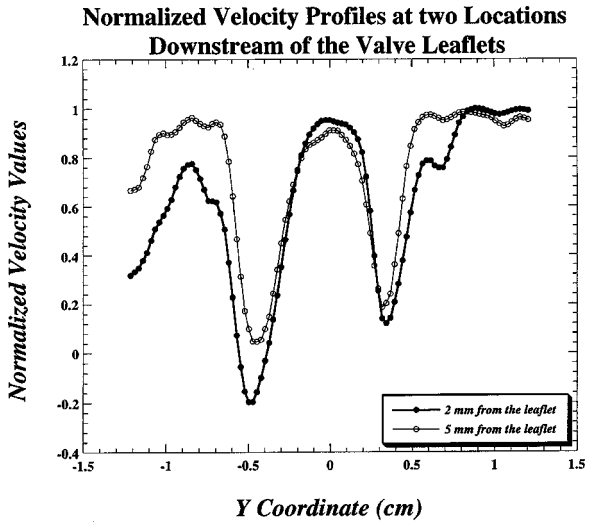

Fig. 13 DPIV measurements of velocity profiles in the wake, distal to the valve

distal to the tip of the leaflet). Taking into account the dynamic nature of vortex shedding, there is a good agreement in the spatial and temporal locales of the vortices, although the numerical results indicate a more elongated structure of the vortices. In Fig. 12 the vorticity distribution along a straight line from the leaflet's tip is depicted. This profile, obtained from the vorticity field, demonstrates the alternating vorticity values of the vortices and their streamwise decay. The vorticity alternated between positive and negative values, typical of the ''Karman vortex street'' dynamics in which successive vortices rotate at alternating clockwise and counterclockwise motion in the wake.

Figure 13 illustrates two different velocity profiles obtained from the DPIV velocity vector field data at two cross sections downstream of the leaflets. The three jets that are formed past the valve; two lateral (between the leaflets and the housing ring) and one central (between the two leaflets), are characteristic of the flow field past bileaflet mechanical prostheses and were in very good agreement with the numerical results. The negative velocity values indicative of the flow reversal adjacent to left leaflet did not appear adjacent to the right leaflet. This could be attributed to a possible misalignment of the flow approaching the leaflets. Since the DPIV images were captured by zooming in very close to the leaflets, the walls of the sinus of Valsalva were excluded from the acquired images. The velocity profiles were obtained at a finite distance from the rigid boundaries, thus not showing velocities approaching zero at the wall. Accordingly, the minimal velocity values in the left hand side of Fig. 5 were in the range of 20–50 cm/s and in the right hand side in the 70–74 cm/s range.

Conclusions

The numerical simulation of unsteady turbulent flow past a bileaflet mechanical heart valves depicted the intricate dynamics of the shed vortices in the wake of the valve's leaflets. The existence of these shed vortices was confirmed in a pulse duplicator system by noninvasive flow measurements using DPIV. It is postulated that these shed vortices provide the optimal conditions for the generation of cerebrovascular microemboli that carry with them the main risk associated with mechanical heart valves, namely, cardioembolic stroke. The ensuing shed vortices provide a semi-closed environment of relatively long lasting ''flow reactors'' wherein blood potentially enriched with platelets leaking mediators is mixed. The shed vortices also provide the flow conditions that promote the formation of larger platelet aggregates, as demonstrated by the vortex pairing phenomenon that happens repeatedly within the wake. Under these flow conditions, cellular and molecular components of the hemostatic system may be brought into repetitive contact with activator molecules and with each other. Following activation, platelets will release their granule constituents and provide procoagulant phospholipid surfaces likely to start the positive feedback reactions of coagulation. Platelet aggregates will increase the efficiency of the reaction, eventually resulting in the formation of free emboli. Once formed, such free emboli would be convected downstream, as demonstrated by the convection of the shed vortices, increasing the risk of systemic emboli. Future work is needed to further establish the effect of these flow dynamics on platelet kinetics and the coagulation cascade. The future work will include studying the stress history of platelets along particular turbulent paths in order to establish the platelet activation state and procoagulant properties, three-dimensional simulations that will incorporate the three-dimensional effects of the shed vortices, *in vitro* measurements of the platelet kinetics in the shed vortices in the wake of the valve, and *in vivo* measurements in animals with implanted MHV's using Transcranial Doppler for establishing correlations between High-Intensity Transient Signals (HITS) and free emboli. Finally, if the current bileaflet MHV designs enhance free emboli formation through the wake of shed vortices generated by the valve, the challenge facing MHV design optimization would be to delineate those design parameters that would reduce or ideally eliminate the formation of shed vortices.

Acknowledgments

This work was supported in part by a grant-in-aid, No. 9706333A from the American Heart Association, New York State Affiliate, Inc. (DB), and by a Scientist Development Grant 9930165N from the American Heart Association (DB).

Nomenclature

CFD = computational fluid dynamics
d = diameter
DPIV = digital particle image velocimetry
f = body forces
g = gram
FFT = fast Fourier transform
k = turbulent kinetic energy
L = liter
MHV = mechanical heart valve
r = radial coordinate
Re = Reynolds number
t = time
u = velocity
U = axial velocity
T = time
x = axial coordinate
ε = viscous dissipation rate of turbulent kinetic energy
μ = viscosity
ν = dynamic viscosity
ρ = density
σ = stress
τ = shear stress
ω = turbulent frequency
$\vec{\omega}$ = vorticity

References

[1] Horstkotte, D., Korfer, R., Seipel, L., Bircks, W., and Loogen, F., 1983, ''Late Complications in Patients With Bjork–Shiley and St. Jude Medical Heart Valve Replacement,'' Circulation, **68**, (Suppl II), pp. 175–184.
[2] Grunkemeier, G. L., and Rahimtoola, S. H., 1990, ''Artificial Heart Valves,'' Annu. Rev. Med., **41**, pp. 251–263.
[3] National Heart, Lung and Blood Institute Working Group on Blood Material Interactions, 1985, Guidelines for Blood–Material Interactions,'' Bethesda, MD, NIH Publication No. 85-2185.
[4] Gerrard, J. M., and White, J. M., 1976, ''The Structure and Function of Platelets With Emphasis on Their Contractile Nature,'' in: *Pathology Annual*, H. L. Iochain, ed., Appleton Century Crofts, New York, pp. 31–58.

[5] Figliola, R. S., and Mueller, T. J., 1981, ''On the Hemolytic and Thrombogenic Potential of Occluder Prosthetic Heart Valves From in Vitro Measurements,'' ASME J. Biomech. Eng., **103**, pp. 83–90.
[6] Baldwin, J. T., Tarbell, J. M., Deutsch, S., and Geselowitz, D. B., 1991, ''Mean Velocities and Reynolds Stresses Within Regurgitant Jets Produced by Tilting Disk Valves,'' ASAIO Trans., **37**, No. 3, pp. M348–M349.
[7] Reif, T. H., Schulte, T. J., and Hwang, N. H. C., 1990, ''Estimation of the Rotational Undamped Natural Frequency of Bileaflet Cardiac Valve Prostheses,'' ASME J. Biomech. Eng., **112**, pp. 327–332.
[8] Lee, C. S., and Chandran, K. B., 1995, ''Numerical Simulation of Instantaneous Backflow Through Central Clearance of Bileaflet Mechanical Heart Valves at Closure: Shear Stress and Pressure Fields Within Clearance,'' Med. Biol. Eng. Comput., **33**, No. 3, pp. 257–263.
[9] Lamson, T. C., Rosenberg, G., Geselowitz, D. B., Deutsch, S., Stinebring, D. R., Frangos, J. A., and Tarbell, J. M., 1993, ''Relative Blood Damage in the Three Phases of a Prosthetic Heart Valve Flow Cycle,'' ASAIO J., **39**, No. 3, pp. M626–M6233.
[10] Harker, L. A., and Slichter, S. J., 1970, ''Studies of Platelet and Fibrinogen Kinetics in Patients With Prosthetic Heart Valves,'' N. Engl. J. Med., **283**, pp. 1302–1305.
[11] Edmunds, Jr., L. H., 1987, ''Thrombotic and Bleeding Complications of Prosthetic Heart Valves,'' Ann. Thoracic Surgery, **44**, No. 4, pp. 430–445.
[12] Dewanjee, M. K., 1990, ''Quantitation of Platelet Thrombus in Cardiac Valve Prostheses With the Radiolabeled Platelets,'' in: *Platelets and Atherosclerosis*, X. Y. Kessler, ed., Springer-Verlag, Berlin–Heidelberg, pp. 71–86.
[13] Turitto, V. T., Weiss, H. J., Baumgartner, H. R., Badimon, L., and Fuster, V., 1987, ''Cells and Aggregates at Surfaces,'' in: *Blood Contact With Artificial Surfaces*, E. F. Leonard, V. T. Turitto, and L. Vroman, eds., New York Academy of Science, New York, Vol. 516, pp. 453–467.
[14] Lelah, M. D., Lamprecht, L. K., and Cooper, S. L., 1984, ''A Canine Ex Vivo Series Shunt for Evaluating Thrombus Deposition on Polymer Surfaces,'' J. Biomed. Mater. Res., **18**, pp. 475–496.
[15] Wurzinger, L. J., Blasberg, P., and Schmid-Schönbein, H., 1985, ''Towards a Concept of Thrombosis in Accelerated Flow: Rheology, Fluid Dynamics, and Biochemistry,'' Biorheology, **22**, pp. 437–449.
[16] Folie, B. J., and McIntire, L. V., 1989, ''Mathematical Analysis of Mural Thrombogenesis: Concentration Profiles of Platelet-Activating Agents and Effects of Viscous Shear Flow,'' Biophys. J., **56**, pp. 1121–1141.
[17] Schoephoerster, R. T., Oynes, F., Nunez, H., Kapadvanjwala, M., and Dewanjee, M. K., 1993, ''Effects of Local Geometry and Fluid Dynamics on Regional Platelet Deposition on Artificial Surfaces,'' Arterioscler. Thromb., **12**, pp. 1806–1813.
[18] Alveriadou, B. R., Moake, J. L., Turner, N. A., Ruggeri, Z. M., Folie, B. J., Phillips, M. D., Schreiber, A. B., Hrinda, M. E., and McIntire, L. V., 1993, ''Real-Time Analysis of Shear Dependent Thrombus Formation and Its Blockade by Inhibitors of Von Wilebrand Factor Binding to Platelets,'' Blood, **81**, pp. 1263–1276.
[19] Hellums, J. D., Peterson, D. M., Stathopoulos, N. A., Moake, J. L., and Giorgio, T. D., 1987, ''Studies on the Mechanisms of Shear-Induced Platelet Activation,'' in: *Cerebral Ischemia and Hemorheology*, A. Hartman and W. Kuschinsky, eds., Springer-Verlag, New York, pp. 80–89.
[20] Sutera, S. P., Nowak, M. D., Joist, J. H., Zeffren, D. J., and Bauman, J. E., 1988, ''A Programmable, Computer-Controlled, Cone-Plate Viscometer for the Application of Pulsatile Shear Stress to Platelet Suspensions,'' Biorheology, **25**, pp. 449–459.
[21] Purvis, N. B., and Giorgio, T. D., 1991, ''The Effects of Elongational Stress Exposure on the Activation and Aggregation of Blood Platelets,'' Biorheology, **28**, pp. 355–367.
[22] Bluestein, D., Niu, L., Schoephoerster, R. T., and Dewanjee, M. K., 1997, ''Fluid Mechanics of Flow Through a Stenosis: Relationship to the Development of Mural Thrombus,'' Ann. Biomed. Eng., **25**, No. 2, pp. 344–356.
[23] Hoerner, S. F., 1958, *Fluid Dynamic Drag*, published by the author, New Jersey.
[24] Hussain, A. K. M. F., 1983, ''Coherent Structures—Reality and Myth,'' Phys. Fluids, **26**, No. 10, pp. 2816–2850.
[25] Hussain, A. K. M. F., 1986, ''Coherent Structures and Turbulence,'' J. Fluid Mech., **173**, pp. 303–356.
[26] Hussain, A. K. M. F., 1975, ''Mechanics of Pulsatile Flows of Relevance to the Cardiovascular System,'' in: *Cardiovascular Flow Dynamics and Measurements*, N. H. C. Hwang and N. A. Norman, eds., University Park Press, Baltimore, MD, Chap. 15, pp. 541–633.
[27] Gross, J. M., Shermer, C. D., and Hwang, N. H. C., 1988, ''Vortex Shedding in Bileaflet Heart Valve Prosthesis,'' ASAIO Trans., **34**, No. 3, pp. 845–850.
[28] Huang, Z. J., Merkle, C. L., Abdallah, S., and Tarbell, J. M., 1994, ''Numerical Simulation of Unsteady Laminar Flow Through a Tilting Disk Heart Valve: Prediction of Vortex Shedding,'' J. Biomech., **27**, No. 4, pp. 391–402.
[29] Merrill, E. W., Gilliland, E. R., Cokelet, G. R., Shin, H., Britten, A., and Wells, R. E., 1963, ''Rheology of Human Blood, Near and at Zero Flow,'' Biophys. J., **3**, pp. 199–213.
[30] Saad, Y., and Schultz, M. H., 1983, ''GMRES: A Generalized Minimal Residuals Algorithm for Solving Nonsymmetric Linear Systems,'' Math. Comput., **44**, pp. 417–424.
[31] Wilcox, D. C., 1993, *Turbulence Modeling for CFD*, DCW Industries, Inc., 5354 Palm Drive, La Cañada, CA 91011.
[32] Wilcox, D. C., 1994, ''Simulation of Transition With a Two-Equation Turbulence Model,'' AIAA J., **32**, No. 2, pp. 247–255.
[33] Gosman, A. D., and Ioannides, L., 1981, ''Aspects of Computer Simulation of Liquid-Fueled Combustors,'' AIAA 19th Aerospace Meeting, Paper No. 81-0323, St. Louis, MO.
[34] Willert, C. E., and Gharib, M., 1991, ''Digital Particle Image Velocimetry,'' Exp. Fluids, **10**, pp. 181–193.
[35] Bellhouse, B. J., and Bellhouse, F. H., 1968, ''Mechanism of Closure of the Aortic Valve,'' Nature (London), **217**, pp. 86–87.